SIMULATION OF PUNCHING FAILURE IN REINFORCED-CONCRETE STRUCTURES

By P. Menétrey,[1] R. Walther,[2] T. Zimmermann,[3] K. J. Willam,[4] and P. E. Regan[5]

ABSTRACT: A numerical model has been developed to reproduce the punching failure in reinforced-concrete structures. It is characterized by an efficient triaxial strength criterion for concrete, a nonassociated flow rule reproducing the concrete dilatancy observed experimentally, and a cracking model accounting for the brittleness of concrete failure under various states of stress. The simulation of punching failure in a circular slab is successfully performed as the localized mode of failure—characterized by an inclined crack—is reproduced. It is shown that punching failure is initiated by the coalescence of microcracks inside the slab, followed by a crack propagation towards the corner of the slab-column intersection. A parametric analysis of the punching failure demonstrates that (1) punching failure is due to tensile failure of concrete along the inclined punching crack and is not due to compressive failure; (2) increasing the percentage of reinforcement reduces the state of internal cracking resulting in an increase of the failure load and a reduction of the ductility; and (3) the size effect observed experimentally is reproduced and a size-effect law is proposed.

INTRODUCTION

Reinforced-concrete slabs supported on columns fail by punching when a column suddenly perforates the slab with the formation of a conical plug of concrete. A review of this failure phenomenon has been presented by Regan and Braestrup (1985). The approach adopted here is concerned with the finite-element simulation of this failure mechanism using a triaxial concrete formulation.

Punching failure in reinforced-concrete slabs under dynamic impacts or under static loading was simulated with different concrete models in which the size effect was usually neglected. The first attempt to apply fracture mechanics to punching failure is reported by De Borst and Nauta (1985). A model handling nonorthogonal cracks was used and the predicted behavior approached experimental results. However, the tangential cracks spread and no localized punching mode was generated.

The finite-element simulation of punching failure in reinforced-concrete structures is a promising approach that should provide new insight into the failure mechanism. To reproduce more closely the punching failure process, a review of the experimental tests published in the literature was performed, leading to the following requirements for the numerical model:

1. The punching failure involves tangential cracks as well as radial cracks. Consequently the numerical model must be able to manage these two types of cracks.
2. Shear and flexural effects interact and cannot be considered separately. Consequently, a continuum model should be developed as opposed to a structural one.
3. Punching failure is a highly localized failure and is not a diffuse failure. Therefore, the numerical model should capture strain localization.
4. Punching failure exhibits size effects that can be properly accounted for by nonlinear fracture mechanics concepts.
5. The influence of flexural reinforcement is prominent. Therefore, a discrete idealization of the reinforcement, as opposed to embedded composite models, should be considered so that yielding and debonding can be captured.

After conducting this review, it appeared that the following assumptions were appropriate and, therefore, are adopted here: (1) punching failure is a three-dimensional failure phenomenon that may be simulated as axisymmetric; and (2) the dowel action (shear resistance transferred by reinforcing bars crossing a concrete interface), which influences the response of reinforced-concrete slabs near the peak load, can be neglected.

A numerical model that satisfies these requirements is derived in the next section. In the third section, the punching failure mechanisms are investigated. In the fourth section, a parametric analysis of punching failure is presented. Further details are given in Menétrey (1994).

NUMERICAL MODEL

Preliminaries

The reinforced-concrete behavior is described at the constitutive level within the framework of the incremental flow theory of plasticity [see e.g., Chen (1982)], assuming that the elastic and plastic strain increments are uncoupled: $\Delta\boldsymbol{\varepsilon} = \Delta\boldsymbol{\varepsilon}_e + \Delta\boldsymbol{\varepsilon}_p$. The actions of steel reinforcement and concrete are uncoupled. The steel model is characterized by a bilinear stress-strain response and a symmetric response under tension and compression.

Concrete Failure Criterion

The concrete failure criterion is necessary to describe punching failure as mentioned by Moe (1961). An appropriate triaxial strength criterion developed by Menétrey and Willam (1995) is used here to reproduce the various states of stress characterizing punching failure. It is expressed in terms of the three invariants I_ξ, I_ρ, and I_θ [hydrostatic, deviatoric invariant, and polar angle of Haigh-Westergaard, see e.g., Chen (1982)] of the stress tensor $\boldsymbol{\sigma}$ as

$$f(I_\xi, I_\rho, I_\theta) = \left[\sqrt{1.5}\,\frac{I_\rho}{f_c}\right]^2 + \phi\left[\frac{I_\rho}{\sqrt{6}f_c}\,r(I_\theta, e) + \frac{I_\xi}{\sqrt{3}f_c}\right] - c = 0 \tag{1}$$

[1]Res. Asst., Dept. of Civ. Engrg., Ecole Polytechnique Fédérale de Lausanne, CH-1015 Lausanne, Switzerland.

[2]Prof. Emeritus, Dept. of Civ. Engrg., Ecole Polytechnique Fédérale de Lausanne, CH-1015 Lausanne, Switzerland.

[3]Lect., Dept. of Civ. Engrg., Ecole Polytechnique Fédérale de Lausanne, CH-1015 Lausanne, Switzerland.

[4]Prof., Dept. of Civ. Engrg., Univ. of Colorado at Boulder, Boulder, CO 80309.

[5]Prof., School of Arch. and Engrg., Univ. of Westminster, London, NW1 5LS, England.

Note. Associate Editor: John B. Mander. Discussion open until October 1, 1997. To extend the closing date one month, a written request must be filed with the ASCE Manager of Journals. The manuscript for this paper was submitted for review and possible publication on January 15, 1996. This paper is part of the *Journal of Structural Engineering*, Vol. 123, No. 5, May, 1997. ©ASCE, ISSN 0733-9445/97/0005-0652–0659/ $4.00 + $.50 per page. Paper No. 10453.

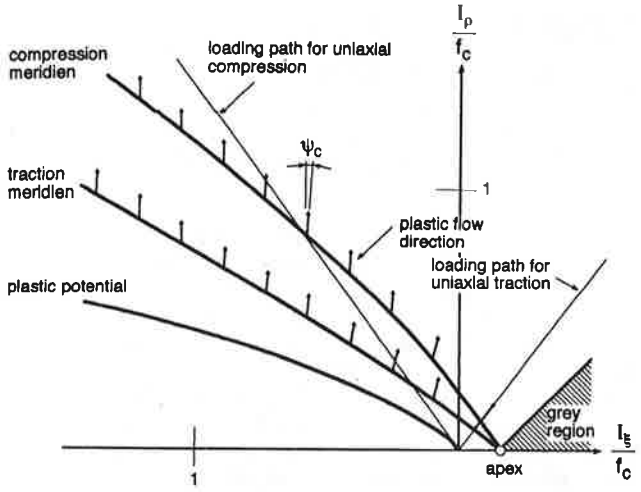

FIG. 1. Concrete Failure Criterion, Plastic Potential, Plastic Flow Direction, and Grey Region in the Meridian Plane

where f_c = uniaxial compressive strength. The cohesive parameter is set to $c = 1$ and the friction parameter is $\phi = 3[(f_c^2 - f_t^2)/(f_c f_t)(e)/(e + 1)]$ where f_t =uniaxial tensile strength. The elliptic function $r(I_\theta, e)$ is based on the five-parameter model by Willam and Warnke (1974)

$$r(I_\theta, e) = \frac{4(1 - e^2)\cos^2 I_\theta + (2e - 1)^2}{2(1 - e^2)\cos I_\theta + (2e - 1)[4(1 - e^2)\cos^2 I_\theta + 5e^2 - 4e]^{1/2}} \quad (2)$$

The parameter e describes the out of roundness of the deviatoric trace, which is expressed as the limit of the ratio of the tensile meridian ($I_\theta = 0$) over the compressive meridian ($I_\theta = \pi/3$) as I_ρ tends to 0. Convexity and smoothness of the elliptic function require that $0.5 < e \leq 1$. One singular apex, if $\phi > 0$, is located at: $[I_\xi = (c\sqrt{3}f_c)/\phi, I_\rho = 0]$. The failure criterion in the meridian plane along the tensile ($I_\theta = 0$) and the compressive ($I_\theta = \pi/3$) meridians, as well as the apex, are shown in Fig. 1.

Concrete Flow Rule

The evolution of plastic deformation is described with a flow rule derived from the plastic potential g such that: $\Delta\boldsymbol{\varepsilon}_p = \Delta\gamma\partial g/\partial\boldsymbol{\sigma}$ ($\Delta\gamma$ = plastic multiplier; and ∂ = partial derivative). The plastic potential, which was appropriated to simulate punching failure is expressed as

$$g(I_\rho, I_\xi) = I_\rho^2 + BI_\rho + CI_\xi \quad (3)$$

where parameters B and C outline the axisymmetric shape as presented in Appendix I. The plastic potential satisfies the following two conditions: (1) for uniaxial tensile test, the flow direction corresponds to the loading path for uniaxial tension (this condition reproduces, during the uniaxial tensile test of a plain concrete specimen, the elastic unloading in the radial direction observed experimentally); and (2) at the uniaxial ultimate compressive strength, the flow direction is given by the dilatancy angle ψ_c, introduced as a new material parameter. These two conditions are presented in Fig. 1.

The shape of the plastic potential is circular in the deviatoric plane, which corresponds to a nonassociated flow rule except if $e = 1$. This assumption, which simplifies the formulation and facilitates the stress computation, is neither contradicting nor reproducing experimental results, as very few are available.

The apex of the failure criterion results in a grey region in the stress space where the stress return algorithm is not defined. This grey region is illustrated in Fig. 1 and is delimited by the condition

$$I_\xi \leq I_\rho \frac{C}{B} + \frac{c\sqrt{3}f_c}{\phi} \quad (4)$$

If the stress state is located in the grey region, it is returned to the apex of the failure criterion.

Concrete Cracking

The concrete cracking phenomenon is described with the smeared-crack model using the strain-softening formulation that refers to a gradual decrease in tensile strength with additional deformation. The fictitious crack model developed by Hillerborg et al. (1976) is considered, in which the tensile stress σ_t is controlled by the crack opening w. The amount of energy per unit area absorbed in opening a crack from zero to the crack rupture opening w_r is

$$G_f = \int_0^{w_r} \sigma_t \, dw \quad (5)$$

defining the fracture energy, which is considered a material property.

The gradual decrease in tensile strength with additional deformation is controlled by a smooth exponential degradation of the cohesive parameter in order to fit the tensile experimental data, which dominates the postpeak response of concrete, so that

$$c = \frac{\sigma_t}{f_t} = \exp\left(-5\frac{w}{w_r}\right) \quad (6)$$

The cohesive parameter is uncoupled in the expression of the concrete failure criterion given in (1), resulting in an isotropic loss of strength due to reduction of the cohesion. For $c = 1$, the material is intact, and for $c = 0$, the material is considered to be completely fractured exhibiting only a residual frictional strength.

The fracture energy must be invariant with the finite-element size. Therefore, mapping between the crack opening w (used for the definition of the constant fracture energy) and the cracking strain ε_c (used at the constitutive level) leads to the definition of the finite-element size h^e normal to the crack, so that $w = h^e\varepsilon_c$ following the idea of the crack band model by Bažant and Oh (1983). The simulation of localized failure, like punching failure, requires this dependence on finite-element size, which plays the role of localization limiter.

The punching-failure process is characterized by distinct states of stress for which different brittleness behaviors are associated. These different brittleness behaviors are included in the model by considering the number of microcracks formed in a specimen, following the experimental observations that splitting in compression, as well as shear, results from various microcracks. The analytical formulation of the fictitious number of cracks N is derived based on the following experimental observations: (1) the uniaxial tensile ($I_\xi = f_t/\sqrt{3}, I_\rho = \sqrt{2/3}f_t, I_\theta = 0$) and the triaxial extension tests ($I_\xi = \sqrt{3}f_t, I_\rho = I_\theta = 0$) are characterized by one single crack; (2) the uniaxial compressive test ($I_\xi = -f_c/\sqrt{3}, I_\rho = \sqrt{2/3}f_c, I_\theta = \pi/3$) is characterized by N_b cracks (introduced as a new material parameter); and (3) the biaxial compressive test ($I_\xi = -2f_{bc}/\sqrt{3}, I_\rho = \sqrt{2/3}f_{bc}, I_\theta = 0$), ($f_{bc}$ = equibiaxial compressive strength) is characterized by one crack. For punching failure simulation, the reproduction of the biaxial compressive state of stress is determinant, as is observed at the corner of the slab-column intersection. The analytical expression of the fictitious number of cracks includes the polar angle I_θ in order to distinguish between the localized failure, along the tensile meridian, and the distributed failure along the compressive meridian. The fictitious number of cracks is expressed in terms

of the ratio I_ξ/I_ρ so that it remains constant during proportional unloading. The fictitious number of cracks is written as

$$N = \begin{cases} \sqrt{2}\left(-\frac{I_\xi}{I_\rho} + 1/\sqrt{2}\right)(1 - \cos I_\theta)(N_b - 1) + 1 & \frac{I_\xi}{I_\rho} < 1/\sqrt{2} \\ 1 & \frac{I_\xi}{I_\rho} \geq 1/\sqrt{2} \end{cases} \tag{7}$$

so that the three previously mentioned observations are satisfied.

The combination of radial and tangential cracks is accounted for in an average form by computing the increment of the crack opening Δw as the positive norm of the plastic strain $\|\langle \Delta \boldsymbol{\varepsilon}_p \rangle\|$ (being the internal variable), where $\|\cdot\|$ denotes the square norm, and $\langle\rangle$ are the Macauley brackets, which extract the positive components so that $\langle \mathbf{x} \rangle = \sqrt{0.5(x_i + |x_i|)x_i}$. The increment of the crack opening is consequently expressed as

$$\Delta w = h^e \Delta\gamma \left\| \left\langle \frac{\partial g}{\partial \boldsymbol{\sigma}} \right\rangle \right\| \frac{1}{N} \tag{8}$$

where $\Delta\gamma$ = plastic multiplier.

The stiffness degradation due to cracking is assumed to occur only in the softening range of the response. The elastic constitutive matrix is modified isotropically with a degradation of the initial Young's modulus E_0 so that

$$E = cE_0 \tag{9}$$

For a completely damaged material ($c = 0$) Young's modulus is reduced to zero. This model corresponds to an isotropic damage model and was shown to be necessary to capture the punching failure mechanism.

Numerical Implementation

The stress integration algorithm is based on the elastic-predictor, plastic-corrector strategy. The elastic-predictor step is elastic, and the plastic corrector step is evaluated with the cutting plane algorithm developed by Ortiz and Simo (1986). A relaxation method is coupled with the cutting-plane algorithm to avoid a situation in which the stress point is returned accidentally inside the elastic domain due to the exponential decohesion process.

Circular reinforced-concrete slabs that are modeled with four-node quadrilateral axisymmetric elements (quadaxi) are considered. The regularization parameter of the quadaxi (h^e), which appears in the softening formulation, is the square root of the cross-sectional area so that the radial direction is not taken into account. This results in a constant crack spacing along the perimeter as observed in punching failure experiments.

Mesh locking occurs as a result of near incompressibility. For the developed concrete constitutive model, the flow rule often allows for only small volume changes, so if plastic strains become large, the response becomes nearly incompressible. This difficulty is overcome by the treatment developed by Hughes (1980) using the mean-dilatation formulation.

The nonlinear solution is advanced in incremental load steps and requires iterations. A modified Newton-Raphson algorithm is implemented with a special strategy adapted to capture localized failure so that (1) the predictor iteration is elastic in order to facilitate unloading; (2) the corrector iteration is elastic for a certain number of converging iterations (norm of the out-of-balance force is reducing) and only after these elastic iterations the corrector iteration is plastic; and (3) the corrector iteration is elastic as soon as divergence of the norm of the out-of-balance force is detected.

The damaged elastic constitutive matrix is assumed constant during a load step and is computed at the previous converged step (not at the previous iteration). This has the advantage that no coupling between elastic degradation and plastic softening has to be considered. However, small load steps are required.

PUNCHING FAILURE MECHANISMS

Description of Test Problem

The circular slab tested by Kinnunen and Nylander (1960) and reinforced with ring reinforcement (denoted by IB15a) is simulated because of its perfect axially symmetric geometry. It has a total diameter of 1,840 mm and a thickness of 150 mm. Experimentally, the load is applied to the column (150 mm in diameter) by means of a hydraulic jack and transferred to the floor by means of tie rods along a radius of 855 mm.

The finite-element mesh used for the simulation is chosen such that the punching crack is aligned with the mesh without predefining its orientation. The mesh is refined around the corner of the slab-column intersection. The load is applied by controlling the vertical displacement to follow an eventual softening response.

The concrete is characterized by a mean compressive strength on the cylinder of $f_c = 28$ MPa. The tensile strength is obtained based on the following relation:

$$f_t = 0.33 f_c^{2/3} \tag{10}$$

which results in a direct tensile strength of $f_t = 3$ MPa. The fracture energy—according to the CEB-FIP model code (CEB 1990)—depends on the maximum aggregate size (32 mm) and on tensile strength so that $G_f = 120$ N·m/m^2. The following parameters are assumed: (1) Young's modulus $E_0 = 25{,}000$ MPa; (2) Poisson's ratio = 0.2; (3) the number of cracks in compression $N_b = 10$; and (4) the dilatancy angle is at the ultimate uniaxial compressive strength $\psi_c = 10°$. The reinforcement is made of Swedish Kam steel-ribbed bars 12 mm in diameter, which are characterized by Young's modulus of 210,000 MPa and a uniaxial yield strength of 450 MPa. The hardening modulus is assumed to be 10,000 MPa. The positions of the ring elements are approached so that they are located at the nodes of the concrete finite-element mesh.

Punching Response of Slab

The response of the slab is illustrated in Fig. 2 where the load-displacement curve of the point located at the perimeter of the slab is presented. The predicted punching load (202 kN) agrees with the experimental failure loads (188 and 208 kN). The numerical simulation does not reproduce the five horizontal branches monitored experimentally due to pauses during the load-controlled test without closed-loop systems. This implies that the numerical model predicts a stiffer response than the one monitored experimentally.

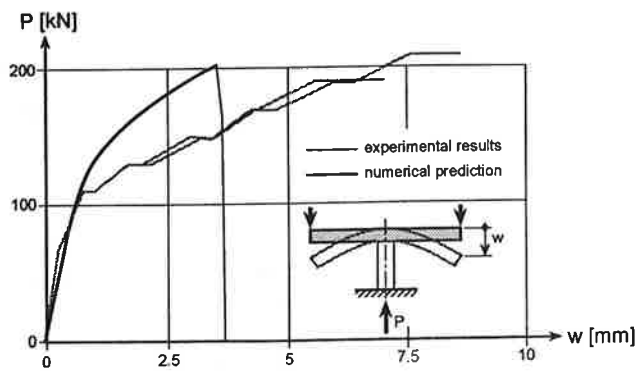

FIG. 2. Experimental and Numerical Responses of Slab with Ring Reinforcement

The deformed mesh of the simulated slab is shown in Fig. 3. A punching mode of failure is reproduced for which the deflections are localized along an inclined band of element.

Cracking Phenomenon

The punching failure simulation illustrates the cracking phenomenon in the vicinity of the column as shown in Fig. 4 for three load steps. The tangential cracks appear if the principal strains are larger than the rupture deformation in uniaxial traction f_t/E_0. The tangential cracks are symbolized by a straight line, the length of which is computed based on the cohesive parameter and the size of the finite element such that crack length = $0.33h^e(1 - c)$. The crack orientation is similar to the principal strain orientation. A stress-free crack is sym-

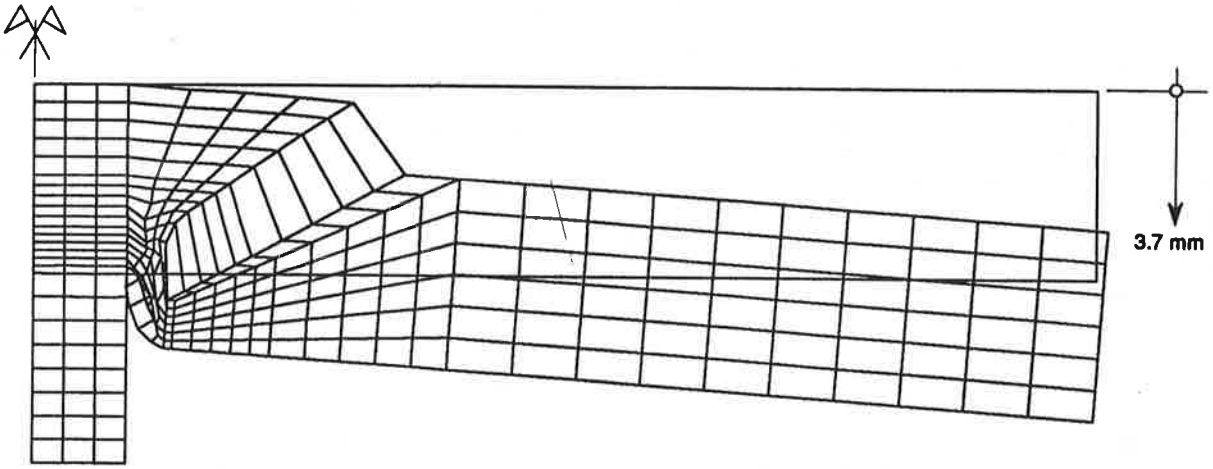

FIG. 3. Deformed Mesh of Slab after Punching Failure

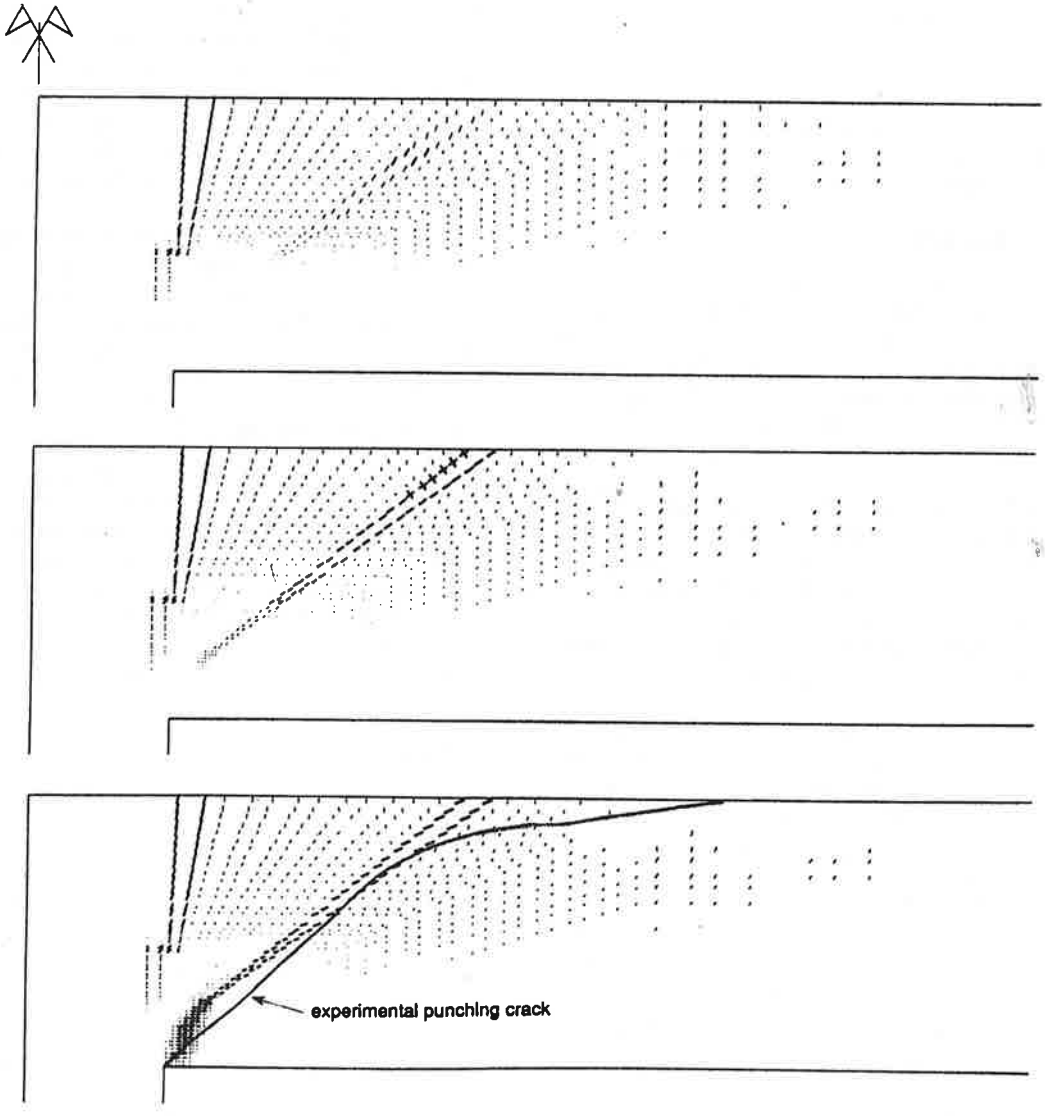

FIG. 4. Tangential Cracks for Three Values of Vertical Displacement: (1) 3.1 mm; (2) 3.2 mm; (3) 3.3 mm

bolized by a thicker line and is represented if $c < 0.007$ (corresponding to $w > w_r$).

Fig. 4 shows that, for a vertical displacement of 3.1 mm corresponding to a stress-free tangential flexural crack opened through half the slab thickness, the first inclined stress-free crack appears inside the slab thickness, just below the reinforcement. The numerous microcracks located around the stress-free crack are closing at that time. The punching crack is initiated by microcrack coalescence at the top of the slab. This coalescence phenomenon is justified experimentally by the tests of Regan (1983), who reported that microcracks are formed across the slab thickness before failure occurs, and Moe (1961), who observed the formation of inclined cracks across the slab thickness before failure occurred. By increasing the vertical displacement, this inclined crack expands toward the corner of the slab-column intersection. Most of the other inclined microcracks are closing at the same time. At failure, the punching crack has reached the corner of the slab-column intersection. The punching crack orientation is close to the experimental one except at the top of the slab. Consequently, punching failure that is initiated by microcrack coalescence is followed by a crack propagation.

The Bažant (1992) suggested that punching failure results only from crack propagation, but the proposed direction of propagation is contrary to the one observed here, as the punching crack is propagating from the upper part of the slab to the bottom.

The formation of radial cracks is well captured by the finite-element model, because the cracks expand towards the extremity of the slab for low load levels as observed experimentally. The main sequence of punching failure mechanisms is consequently reproduced.

PARAMETRIC ANALYSIS

Punching Failure in Slab with Orthogonal Reinforcement

The reference punching failure simulation is performed on a slab similar to the previous one except that the concrete uniaxial compressive strength is $f_c = 28.1$ MPa, the uniaxial tensile strength is $f_t = 3$ MPa, and the slab is reinforced with orthogonal bars 12 mm in diameter and spacing $s = 115$ mm, which are replaced by an equivalent thin steel plate. The percentage of reinforcement ρ—defined as the ratio of the steel to the effective concrete area—allows us to compute the equivalent thickness t of this thin steel plate so that

$$\rho = \frac{2\pi rt}{2\pi rd} = \frac{t}{d} \tag{11}$$

where d = effective depth of the slab; and r = considered radius. The percentage of reinforcement of the reference slab is $\rho = 0.8\%$, which is replaced by a thin steel plate of thickness $t = \rho d = 0.8 \cdot 125 = 1$ mm. This equivalent thin steel plate is modeled with ring and axisymmetric bar elements. The ring elements have approximately the same spacing as the one of the orthogonal reinforcement. They are located at the nodes of the concrete finite-element mesh and have an area that is a function of this spacing s in the form of ts. The axisymmetric bar elements are characterized by their thickness, which is equal to the thickness of the equivalent thin steel plate.

The simulation of punching failure in a slab reinforced with axisymmetric bar elements by assuming a perfect bond between concrete and steel leads to many cracked elements at the interface of the axisymmetric bar elements. The strain localization along one band of element characterizing punching failure is not generated due to diffusion of the force from the steel to the concrete (this diffusion was not observed in the first simulation, as only ring reinforcements were set). Consequently, the perfect bond condition between concrete and steel is relaxed.

The proposed method of relaxing the perfect bond condition and allowing some cracks to grow and others to close involves fastening the steel reinforcement rigidly to the concrete only at the extremity of a fictitious fastening length l_F. This fictitious fastening length is determined by analogy with the crack spacing observed experimentally during a tensile test in reinforced concrete so that the condition

$$h^e < l_F < 2s_{r,m} \tag{12}$$

is satisfied, where $s_{r,m}$ = mean crack spacing in tension; and h^e = finite-element size. The numerical simulation of the reference slab is performed by assuming a fastening length of 75 mm (the fastening length is approximated due to the irregularity of finite-element mesh) along the axisymmetric bar elements. It should be mentioned that the fastening length is a material characteristic.

The punching failure in the reference slab is successfully simulated allowing the parametric analysis to be performed.

Influence of Concrete Characteristics

The concrete parameters, such as the tensile and compressive strengths, are known to be interrelated. However, for the following parametric analysis, they are considered independently in order to determine their effects on the punching failure process.

The influence of the concrete's uniaxial tensile strength is investigated by simulating three slabs with different tensile strengths ($f_t = 2.1$, 3, and 3.9 MPa). The cracking mechanism is analogous for the three slabs but the response curves are distinct as shown in Fig. 5. The behavior of the slab is stiffer for a high value of tensile strength. The load at which the first stress-free tangential flexural crack appears (illustrated by a discontinuity of the response curves) increases with the increasing value of the tensile strength. Once the tangential flexural crack has formed, the slope of the response is similar for all slabs. The failure occurs first in the slab with the lowest tensile strength.

The influence of the uniaxial tensile strength on the punching load (179, 222, and 261 kN) is clearly demonstrated. The result is fitted with simple power functions as they intersect the origin and are commonly used mathematical expressions. The best matching is obtained for

$$P_{\text{failure}} \propto f_t^{2/3} \tag{13}$$

where $\propto$ expresses the proportionality; and P_{failure} = punching load.

The uniaxial concrete compressive strength does not influence the punching failure as neither the cracking mechanism, nor the response curve, are modified for slabs with different

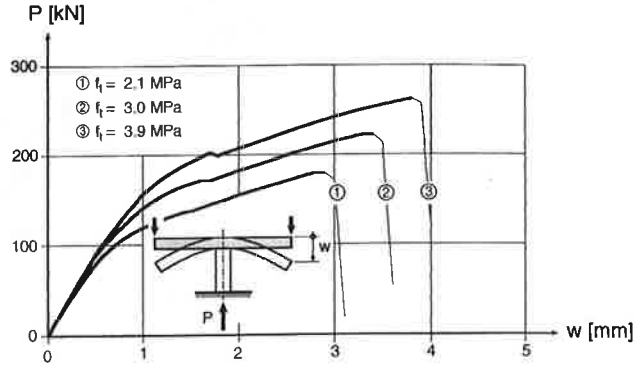

FIG. 5. Influence of Concrete Uniaxial Tensile Strength on Response

uniaxial compressive strengths: f_c = 22.5, 28.1, and 33.7 MPa (when the tensile strength is held constant). It can be concluded that the punching failure is due to tensile failure of concrete along the inclined punching crack and is not due to compressive failure of concrete. The influence of the tensile strength was already suggested by Moe (1961) who noted that the punching failure is very often of a splitting type, and that it is comparable to the type of failure observed in specimens under tension. Consequently, analytical models that assume a compressive failure, such as that by Kinnunen and Nylander (1960), are based on an improbable failure mechanism. They can, however, approximate failure loads because the tensile and compressive strengths of concrete are generally interrelated.

The influence of concrete fracture energy was investigated and it was demonstrated that fracture energy does not influence the stiffness of the behavior, but it influences the ductility as the maximum displacement is increased with increasing fracture energy. The number of cracks in uniaxial compression (N_b = 5, 10, and 15), the out-of-roundness parameter (e = 0.52, 0.55, and 0.6), the Young's modulus (E_0 = 20,000, 25,000, and 30,000 MPa), and the dilatancy angle at the uniaxial ultimate compressive strength (ψ_c = 5°, 10°, and 15°) have little influence on the cracking mechanism and the response curve.

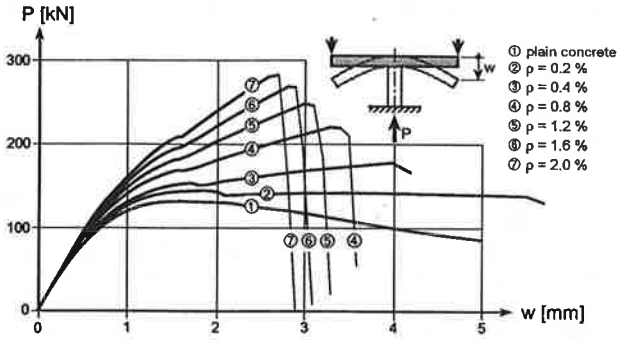

FIG. 6. Influence of the Percentage of Reinforcement on Response

TABLE 1. Influence of Size on the Punching Load and Nominal Shear Stress

h (mm) (1)	d (mm) (2)	r_s (mm) (3)	Slab's diameter (mm) (4)	$P_{failure}$ (kN) (5)	τ_n (MPa) (6)
75	60.5	37.5	855	72	2.8
150	121	75	1,710	222	2.15
300	265	150	3,420	737	1.58
450	397	225	5,130	1,370	1.3

Influence of Reinforcement

The influence of the percentage of reinforcement is studied by simulating slabs with different percentages: ρ = 0.2, 0.4, 0.8, 1.2, 1.6, and 2%. A similar cracking mechanism is observed for all these slabs. The corresponding response curves are presented in Fig. 6 in addition to the one of a flexural failure generated for a plain concrete slab. After a similar initial elastic behavior, the response of the slabs varied tremendously depending on the percentage of reinforcement. When the percentage of reinforcement was increased, the value of the punching load was increased and the ductility was decreased. These results are comparable with the experimental results obtained by Elstner and Hognestad (1956). By increasing the percentage of reinforcement, the state of internal cracking decreases. It should be mentioned that the influence of the dowel force (shear force transferred by reinforcing bars crossing a concrete interface) is not considered in the numerical model.

Size Effect

The size effect is investigated by simulating four slabs of different sizes, but with similar scaling factors applied to the concrete geometry and the steel area, as summarized in Table 1. Except for these dimensions, the slabs have similar boundary conditions and material characteristics. The finite-element mesh is refined for large structures to avoid unstable response as the softening slope is controlled by the finite-element size. The steel fastening length (l_F = 75 mm) is constant from one slab to another. This implies that the nodes at which the steel and the concrete are fastened are different from one slab to another.

The nominal shear stress given in Table 1 is computed as

$$\tau_n = \frac{P_{failure}}{\pi(2r_s + d)d} \qquad (14)$$

where the radius of the column is denoted by r_s; and d = slab effective depth. The nominal shear stress decreases with increasing slab thickness illustrating size effect.

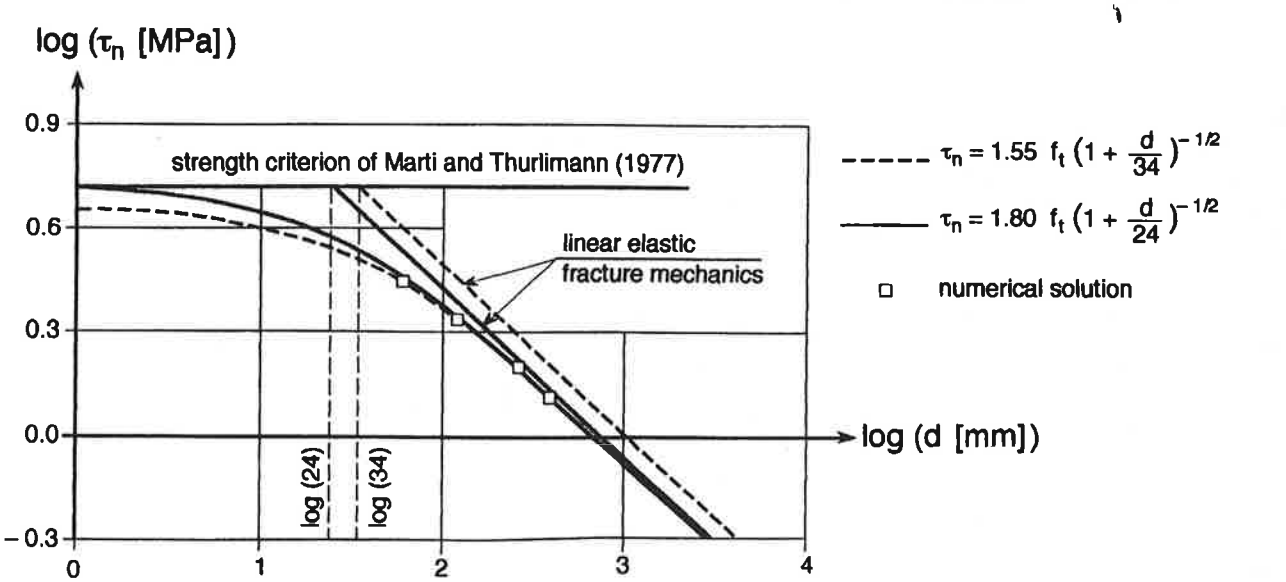

FIG. 7. Size-Effect Law Derived from Numerical Simulations

In assuming a constant fracture energy, Bažant (1984) derived a size-effect law, which was shown to describe the size effect in punching failure shown by Bažant and Cao (1987). It is adjusted based on the four slab simulations (without having the experimental scatter) following the RILEM (1990) recommendations (1990) by linear regression, which gives

$$\tau_n = 1.55 f_t (1 + d/34)^{-1/2} \tag{15}$$

where f_t = uniaxial tensile strength of concrete. This relation is plotted in Fig. 7, in which the two asymptotes: the horizontal (strength criterion) and the inclined (linear elastic fracture mechanic), are distinguished.

Another adjustment of the size-effect law is accomplished by forcing the strength criterion given by the upper-bound load proposed by Marti and Thürlimann (1977). This leads to the following size-effect law:

$$\tau_n = 1.8 f_t (1 + d/24)^{-1/2} \tag{16}$$

This relation is also plotted in Fig. 7. For both proposed laws, the effective depth of the slab is divided by a value that is close to the standard maximal aggregate size of 32 mm.

CONCLUSION

A computational simulation tool has been developed to reproduce punching failure in reinforced-concrete slabs. The developed concrete model is able to simulate punching failure in the following aspects: (1) the different states of stress characterizing punching failure are reproduced with a triaxial failure criterion; (2) the dilatancy observed experimentally is matched with a specific flow rule; and (3) the connection between the brittleness of failure and the state of stress is reproduced by introducing a fictitious number of cracks.

The simulation of punching failure in a circular slab reinforced with ring reinforcement and the comparison with the experimental results reveal that the punching mode of failure, characterized by a localized inclined punching crack, is properly generated. By studying the failure mechanism, it is shown that the punching crack is initiated by a microcrack coalescence phenomenon inside the slab followed by crack propagation towards the corner of the slab-column intersection.

The parametric analysis of the punching failure reveals that: (1) punching failure is due to the tensile failure of concrete along the inclined punching crack and is not due to compressive failure of concrete; (2) the consequence of increasing the percentage of reinforcement is that the state of internal cracking is decreased and the punching load is raised; and (3) the size effect observed experimentally is reproduced numerically and a size-effect law that can be used for design purposes is adjusted to the numerical results.

The proposed computational tool gives deep insight into the failure mechanisms and the parameters influencing the punching failure, which will be useful in design procedures.

ACKNOWLEDGMENTS

Financial support was provided by "La fondation pour la recherche scientifique et systématique dans les domaines de la construction en béton et béton armé de la Société suisse des fabricants de ciment, chaux et gypse." Thanks go to J.-C. Reymond for drawing the figures.

APPENDIX I. DERIVATION OF FLOW RULE

The plastic potential g monitoring the flow rule is expressed as

$$g(I_\rho, I_\xi) = I_\rho^2 + BI_\rho + CI_\xi \tag{17}$$

The plastic flow direction is the gradient of the plastic potential so that

$$m_{ij} = \frac{\partial g}{\partial \sigma_{ij}} = \left(2 + B\frac{1}{I_\rho}\right) s_{ij} + \frac{C}{\sqrt{3}}\delta_{ij} \tag{18}$$

It depends on the deviatoric stress tensor $\mathbf{s}$ with a constant volumetric component. The parameters B and C are determined so that the dilatancy of the plastic strains observed in triaxial experiments is reproduced. The following two conditions are satisfied: (1) for the uniaxial tensile test, the flow direction is equal to the loading path for uniaxial tension (this condition reproduces the elastic unloading in the radial direction observed experimentally during a uniaxial tensile test in plain concrete); (2) at the uniaxial ultimate compressive strength, the flow direction is given by the dilatancy angle ψ_c introducing a new material parameter. The first condition is satisfied if the slope of the loading path for uniaxial tension ($I_\xi/I_\rho = 1/\sqrt{2}$) equals the flow direction at the ultimate uniaxial tensile strength point ($I_\xi = f_t/\sqrt{3}$, $I_\rho = \sqrt{2/3} f_t$, $I_\theta = 0$). The slope of the flow direction is derived from equation 18 by expressing the invariants: $I_\xi(\mathbf{m}) = C$ and $I_\rho(\mathbf{m}) = 2I_\rho + B$ so that the first condition gives

$$\frac{I_\xi}{I_\rho} = \frac{C}{2I_\rho + B} = \frac{1}{\sqrt{2}} \tag{19}$$

This condition must be valid at the uniaxial tensile strength point, leading to

$$\frac{2}{\sqrt{3}} f_t + \frac{1}{\sqrt{2}} B = C \tag{20}$$

The second condition states that at the uniaxial ultimate compressive strength point, ($I_\xi = -f_c/\sqrt{3}$, $I_\rho = \sqrt{2/3} f_c$, $I_\theta = \pi/3$), the flow direction is given by the dilatancy angle ψ_c. This second condition is expressed as $\tan \psi_c = I_\xi/I_\rho$, and introducing the invariants of the flow rule leads to

$$\frac{2\sqrt{2}}{\sqrt{3}} \tan \psi_c f_c + \tan \psi_c B = C \tag{21}$$

Combining 20 and 21 leads to

$$B = \frac{2(\sqrt{2} \tan \psi_c f_c - f_t)}{\sqrt{3}(1/\sqrt{2} - \tan \psi_c)}; \quad C = \frac{1}{\sqrt{2}} B + \frac{2}{\sqrt{3}} f_t \tag{22, 23}$$

The parameter B must remain strictly positive which implies that

$$\arctan\left(\frac{f_t}{\sqrt{2} f_c}\right) < \psi_c < \arctan\frac{1}{\sqrt{2}} \approx 35.3° \tag{24}$$

for $f_c/f_t = 10$ this condition reads: $4° < \psi_c < 35.3°$.

APPENDIX II. REFERENCES

Bažant, Z. P. (1984). "Size effect in blunt fracture: concrete, rock, metal." *J. Engrg. Mech.*, ASCE, 110(4), 518–535.

Bažant, Z. P. (ed.) (1992). *Fracture mechanics of concrete structures: part I, state-of-art report*. ACI Committee 446, Fracture Mechanics, Am. Concrete Inst., Detroit, Mich.

Bažant, Z. P., and Cao, Z. (1987). "Size effect in punching shear failure of slabs." *ACI Struct. J.*, 84, 44–53.

Bažant, Z. P., and Oh, B. H. (1983). "Crack band theory for fracture of concrete." *Matériaux et Constructions*, 16(93), 155–177.

Chen, W. F. (1982). *Plasticity in reinforced concrete*. McGraw-Hill Book Co., Inc., New York, N.Y.

Comité Euro-International du Béton (CEB). (1990). "CEB-FIP model code." *Bull. d'information*, 195–196.

De Borst, R., and Nauta, P. (1985). "Non-orthogonal cracks in a smeared finite element model." *Engrg. Computation*, 2, 35–46.

Elstner, R. C., and Hognestad, E. (1956). "Shearing strength of reinforced concrete slabs." *J. the ACI*, 28(1), 29–58.

Hillerborg, A., Modeer, M., and Petersson, P. E. (1976). "Analysis of crack formation and crack growth in concrete by means of fracture mechanics and finite element." *Cement and Concrete Res.*, 6, 773–782.

Hughes, T. J. R. (1980). "Generalization of selective integration proce-

dures to anisotropic and nonlinear media." *Int. J. Numer. Methods in Engrg.*, 15, 1413–1418.
Kinnunen, S., and Nylander, H. (1960). "Punching of concrete slabs without shear reinforcement." *Trans. 158*, Royal Inst. of Technol., Stockholm, Sweden.
Marti, P., and Thürlimann, B. (1977). "Fliessbedingung für Stahlbeton mit Berücksichtigung der Betonzugfestigkeit." *Bericht 67*, Institut für Baustatik und Konstruktion, Zürich, Switzerland.
Menétrey, P. (1994). "Numerical analysis of punching failure in reinforced concrete structures," PhD thesis, Ecole Polytechnique Fédérale de Lausanne, Lausanne, Switzerland.
Menétrey, P., and Willam, K. J. (1995). "A triaxial failure criterion for concrete and its generalization." *ACI Struct. J.*, 92(3), 311–318.
Moe, J. (1961). "Shearing strength of reinforced concrete slabs and footings under concentrated loads." *Bull. D47*, Portland Cement Assn., Portland, Oreg.
Ortiz, M., and Simo, J. C. (1986). An analysis of a new class of integration algorithms for elastoplastic constitutive relations. *Int. J. Numer. Methods in Engrg.*, 23, 353–366.
Regan, P. E. (1983). "Punching shear in prestressed concrete slab bridges." Tech. Rep., Engrg. Struct. Res. Group, Polytechnic of Central London, London, England.
Regan, P. E., and Braestrup, M. W. (1985). "Punching shear in reinforced concrete." *Bulletin d'information 168*. Comité Euro-International du Béton.
Réunion Internationale des Laboratoires d'Essais et de Recherches surles Materiaux et les Constructions (RILEM). (1990). "Size-effect method for determining fracture energy and process zone size of concrete." *Mat. and Struct.*, Draft Recommendations, 23.
Willam, K. J., and Warnke, E. P. (1974). "Constitutive model for triaxial behavior of concrete." In *Concrete structures subjected to triaxial stresses*. Int. Assoc. for Bridges and Struct. Engrg., Bergamo, Italy.

APPENDIX III. NOTATION

The following symbols are used in this paper:

B, C = parameters of the concrete plastic potential;
E_0, E = initial and damaged Young's modulus of concrete;
G_f = fracture energy;
I_ξ, I_ρ, I_θ = hydrostatic, deviatoric invariants, and polar angle of Haigh-Westergaard;
N = fictitious number of cracks;
N_b = number of fictitious cracks in uniaxial compression;
P = vertical force on a slab;
c = cohesive parameter;
d = slab effective depth;
e = out-of-roundness parameter;
f = failure criterion;
f_c, f_t = uniaxial compressive, tensile strength of concrete;
g = plastic potential;
h^e = finite-element size;
l_F = fastening length between concrete and reinforcement;
$r(I_\theta, e)$ = elliptic function;
r_s = radius of the column;
$\mathbf{s}$ = deviatoric stress tensor;
s, $s_{r,m}$ = reinforcement spacing, mean crack spacing;
t = thickness of steel plate;
w = crack opening;
$\Delta\gamma$ = plastic multiplier;
$\boldsymbol{\varepsilon}$, $\boldsymbol{\sigma}$ = strain, stress tensor;
ϕ = friction parameter;
ψ_c = dilatancy angle at the ultimate uniaxial compressive strength;
ρ = percentage of reinforcement; and
τ_n = nominal stress.

Subscripts

c = crack;
e = elastic;
p = plastic;
r = at rupture; and
t = traction.